The impact of stepwise ionization in a Xe fed electrodeless plasma thruster operation

IEPC-2024-255

Presented at the 38th International Electric Propulsion Conference, Toulouse, France
June 23-28, 2024

J. Zhou* and E. Ahedo†
Department of Aerospace Engineering, Universidad Carlos III de Madrid, Leganes, Spain

and

F. Cichocki‡
Nuclear Department, ENEA, Frascati, Italy

and

F. Taccogna §and P. Minelli ¶
Institue for Plasma Science and Technology ISTP-CNR, Bari, Italy

Abstract: The impact of stepwise ionization is assessed for an electrodeless plasma thruster operated with xenon. Plasma chemistry for the metastable states of xenon, $1s_5$ and $1s_3$, is implemented in a hybrid 2D axisymmetric simulation code. Relevant electron-heavy species collisions are implemented, including excitation from the ground state, relaxation to the ground state, and stepwise ionization. Quenching of the metastable states at the walls is also modeled. Simulations are run for a nominal power of 100W, with the mass flow rate varied between 0.1 and 10mg/s. Injecting more propellant decreases the electron temperature and increases the amount of ions produced from stepwise ionization, being 0.9% for 0.1mg/s and 33.4% for 10mg/s. It is found that once the neutrals are excited to the metastable states, the probability of ionization is >88%, while the negligible relaxation mainly occurs at the walls. For the operation point at 2.5mg/s, by comparing simulations with and without the metastable states, the stepwise ionization is found to improve the propellant utilization by 15% giving rise to a higher thrust efficiency. The metastable neutrals, once generated, are ionized at a distance much shorter than the chamber length and have a negligible density. The ions from stepwise ionization have similar spatial and velocity distributions as those from direct ionization, and account for about 40% of the plasma density.

*Assistant Professor, jzhou@pa.uc3m.es
†Full Professor, eahedo@ing.uc3m.es
‡Permanent Researcher, filippo.cichocki@enea.it
§Senior Researcher, francesco.taccogna@istp.cnr.it
¶Researcher, pierpaolo.minelli@istp.cnr.it

I. Introduction

Electric Propulsion (EP) is substituting Chemical Propulsion for in-space exploration since it offers high specific impulses, and allows significant mass savings of propellant and cost reductions in the mission budget.[1] The mature EP technologies commonly used in space missions are the Gridded Ion Thruster and the Hall Effect Thruster,[2] which make use of electrodes for plasma production and acceleration. These components add complexity to the power control unit, and limit their lifetime due to the erosion caused by the energetic plasma. The novel technologies under research are the electrodeless plasma thrusters (EPTs), such as the Helicon Plasma Thruster (HPT)[3–6] and the Electron Cyclotron Resonance Thruster (ECRT).[7,8] These technologies are based on an antenna for plasma production and a magnetic nozzle for plasma acceleration. The current prototypes still report poor performances at relatively low powers, and upgrades in the existing conventional designs are necessary.[6,8–10] As for propellant, Xe is the preferable one in EP since it is inert, thus minimizing the interactions with the thruster components, and it has a low threshold and a high cross section for ionization, thus optimizing performances. Although alternatives are being searched since its supply is very limited[11–14] and expensive, Xe still represents the baseline propellant.

Theoretical models are extensively used to study the plasma discharge physics in EP technologies.[15–18] The main aspects of the modeling are the plasma dynamics and chemistry (production and interaction with the walls), and the complex plasma-wave interaction in the case of EPTs. The propellant is ionized via collisions with electrons. This production process has inefficiencies since electrons also excite instead of ionizing the propellant, especially at low temperatures,[19] and for atomic propellants such as Xe, this excitation is electronic. Most of the models do not consider the excited states as state-selective, i.e. they are assumed to decay instantaneously to ground state. This is a reasonable assumption for radiative states, which decay very fast (shorter than the electron collisional time) due to spontaneous radiative emission, but not for the metastable states, which can practically decay only via collisions with electrons or after hitting the walls. These excited neutrals in the metastable states could contribute to ionization with mechanisms[19] such as stepwise ionization, i.e. ionization of the excited neutrals via collisions with electrons. The stepwise ionization was recently reported as relevant in EP from theoretical estimations,[20] and experimental measurements.[21]

This work is focused on the study of the stepwise ionization effects on EPTs operated with Xe. For that, a virtual EPT is simulated with HYPHEN, a two-dimensional axisymmetric code with applications for many EP technologies[22–24] and complex chemistry.[25] This code features a hybrid modeling strategy, with a particle-in-cell (PIC) approach for heavy species (neutrals and ions), and a fluid approach for electrons, thus allowing a good trade-off between reliability and computational cost. Simulations consider state-selective the two metastable states of Xe, namely $1s_5$ and $1s_3$,[26] and include both the possible stepwise ionization and the de-excitation processes. Parametric analysis for a varying mass flow and a certain power is conducted to search for regimes where stepwise ionization is important and how it affects the plasma response and performances.

The rest of the work is organized as follows. Section II introduces the plasma chemistry for metastable states and stepwise ionization, the implementation in the hybrid simulation code, and the simulation set-up for the EPT. Section III discusses, for different operation conditions, the relevance and the chemistry of stepwise ionization in the plasma generation. Section IV discusses the impact of stepwise ionization on the plasma discharge. Section V summarizes the conclusions.

II. Methodology

A. Plasma chemistry

Table 1 shows the xenon species considered for the simulations: ground and excited states of the atom and singly ionized state. Ground state is simply noted as Xe, while the electronic excited states are differentiated between radiative ones and the two metastable ones. The former de-excite to the ground state via spontaneous radiative emissions, and are assumed to instantaneously relax to the ground state. For xenon, most of the states are radiative, and the 72 states listed in Ref. 26, at energies levels between 8.44 and 11.58 eV, are considered and are denoted generically as Xe^{**}. The latter relax via collisions with electrons or after hitting the walls, and are tracked in the simulations. For xenon, the two metastable states are $1s_5$ and $1s_3$ at, respectively, energy levels 8.32 and 9.45 eV,[26] and are noted as $Xe^*(1s_5)$ and $Xe^*(1s_3)$ by using the Paschen spectroscopic notation. Regarding the electronic states of the tracked single ion, only the ground state at energy level 12.13 eV is considered, and is noted as Xe^+.

The 38th International Electric Propulsion Conference, P. Baudis Convention Center, Toulouse, France, June 23-28, 2024

Species	**Energy level** [eV]	**Remarks**
Xe	0	
$Xe^*(1s_5)$	8.32	Metastable
$Xe^*(1s_3)$	9.45	Metastable
Xe^{**}	8.44-11.58	Radiative
Xe^+	12.13	

Table 1. Xenon species considered in the model.

Table 2 shows the electron-induced collisions simulated into the model with the data of the corresponding cross sections. Only collisions between electrons and heavy species are considered. Excitation from ground to metastable states and radiative states, de-excitation from metastable states to ground, single direct ionization from ground and single stepwise ionization from mestatable states and elastic collision are simulated. The energy gain or loss for these collisions is the difference between the levels of the initial and final states being a loss for the excitation and ionization and a gain for the de-excitation. Excitation data from ground to metastable states and radiative states is from Ref. 26. De-excitation cross-section data from metastable states to ground are obtained by applying the principle of detailed balance as:[19]

$$\sigma_{deexc}\left(\varepsilon\right) = \frac{g^*}{g}\frac{\varepsilon+\varepsilon_{th}}{\varepsilon}\sigma_{exc}\left(\varepsilon+\varepsilon_{th}\right), \tag{1}$$

where σ_{deexc} and σ_{exc} are the cross sections for de-excitation and excitation, respectively, dependent on the impact energy of the collision ε; ε_{th} is the energy loss of the excitation process ($\varepsilon_{th} = 8.32$eV for $1s_5$ and $\varepsilon_{th} = 9.45$eV for $1s_3$); g and g^* are the degeneracies of the ground state ($g = 1$) and excited state ($g^* = 5$ for $1s_5$ and $g^* = 1$ for $1s_3$),[27] respectively. Direct ionization data is from Ref. 28. Stepwise ionization data is from Ref. 29. Elastic collision data is from Ref. 30.

Number	**Label**	**Collision**	**Energy loss** ε_{th} [eV]	**Remarks**	**Ref.**
1	exc	$e+Xe \rightarrow e+Xe^{**}$	8.44-11.58	Excitation (radiative)	26
2	excm1 ($1s_5$)	$e+Xe \rightarrow e+Xe^*(1s_5)$	8.32	Excitation (metastable)	26
3	excm2 ($1s_3$)	$e+Xe \rightarrow e+Xe^*(1s_3)$	9.45	Excitation (metastable)	26
4	deexc1 ($1s_5$)	$e+Xe^*(1s_5) \rightarrow e+Xe$	-8.32	De-excitation	
5	deexc2 ($1s_3$)	$e+Xe^*(1s_3) \rightarrow e+Xe$	-9.45	De-excitation	
6	dion	$e+Xe \rightarrow 2e+Xe^+$	12.13	Direct ionization	28
7	sion1 ($1s_5$)	$e+Xe^*(1s_5) \rightarrow 2e+Xe^+$	3.81	Stepwise ionization	29
8	sion2 ($1s_3$)	$e+Xe^*(1s_3) \rightarrow 2e+Xe^+$	2.68	Stepwise ionization	29
9	ela	$e+Xe \rightarrow e+Xe$	0	Elastic collision	30

Table 2. Simulated collisions between electron and xenon species, and reference of the cross section data.

In the hybrid plasma model discussed next, rates are used instead of cross sections. Therefore, the velocity distribution functions (VDFs) of the colliding species are needed in principle. For heavy species, the velocities are assumed negligible compared with those of the electrons, which are assumed to follow a Maxwellian VDF. Thus, for a generic collision process c, the collision rate is

$$R_c(T_e) = \sqrt{\frac{8}{\pi m_e T_e^3}}\int_{\varepsilon_{th,c}}^{\infty}\varepsilon\sigma_c(\varepsilon)\exp(-\frac{\varepsilon}{T_e})d\varepsilon, \tag{2}$$

where m_e is the electron mass and T_e the electron temperature. Coulomb collisions, which are not shown in the previous tables are also simulated using the well-known analytical formula for its collision rate.[31]

Figure 1 shows the collision rates for the different collisional processes. The main range of interest for EPTs is, say, between 1 and 20 eV.[32] For excitation, the total rate considering all the possible states is shown and at low T_e, about $T_e \leq 8$ eV, it is larger than that for direct ionization up to some orders of magnitude. The rates for metastable states are negligible compared with the total one, except at very low T_e, about $T_e = 1$ eV, where they contribute to about 10-30%. The rates for stepwise ionization have approximately the same shape as that for the direction ionization, but displaced to lower T_e according to the energy levels of the metastable states. The de-excitation is negligible compared with stepwise ionization in the range of interest.

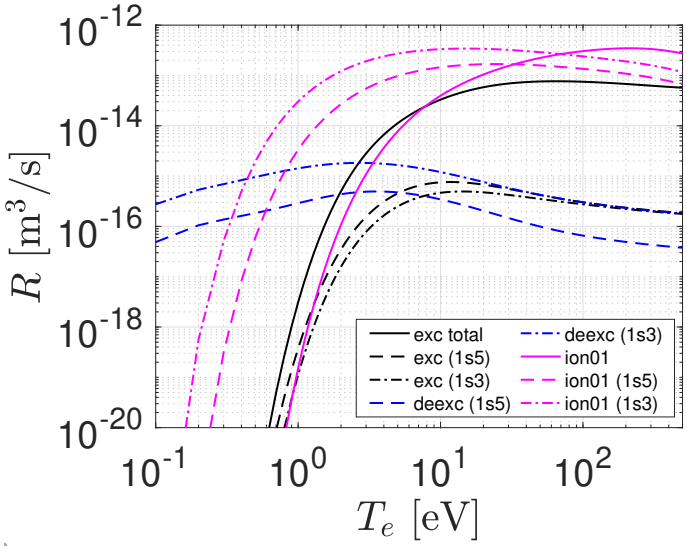

Figure 1. Collision rates for xenon.

B. Simulation model

The simulation tool used in this work for solving the plasma discharge is HYPHEN,[25,33] which implements a 2D axisymmetric hybrid plasma model: a PIC model is used for heavy species and a fluid model for electrons. The output of the PIC model is the heavy species density n_s and mean velocity and $\boldsymbol{u}_s$ with s one of the tracked xenon species (Xe, Xe*(1s$_5$), Xe*(1s$_3$) and Xe$^+$). The output of the fluid model is the electron density n_e, electric potential ϕ, electron velocity $\boldsymbol{u}_e$ and electron temperature T_e. For details about the tool, the reader is referred to Refs. 25,33. Next, some basics of the plasma model, and the treatment of the plasma chemistry of interest here are discussed.

In the PIC model,[34,35] dedicated population lists of macroparticles are used for the tracked species. Macroscopic magnitudes of these species are computed over a structured Cartesian-type mesh from the discrete distribution of macroparticles. Three algorithms are used to solve the heavy species: a particle mover solves for the trajectories of the macroparticles; a collision operator solves for the collisions of the macroparticles; and a surface interaction operator solves for the interaction of the macroparticles with the walls. The plasma chemistry affects the collision and surface interaction operators. The collisions with electrons generate or eliminate heavy species, and for a time step Δt and a cell of volume V_c, the changes in the masses of the species are

$$\Delta m_{Xe} = \left[-\left(R_2 + R_3 + R_6\right) n_{Xe} + R_4 n_{Xe^*(1s_5)} + R_5 n_{Xe^*(1s_3)}\right] n_e m_{Xe} V_c \Delta t, \tag{3}$$

$$\Delta m_{Xe^*(1s_5)} = \left[R_2 n_{Xe} - \left(R_4 + R_7\right) n_{Xe^*(1s_5)}\right] n_e m_{Xe} V_c \Delta t, \tag{4}$$

$$\Delta m_{Xe^*(1s_5)} = \left[R_3 n_{Xe} - \left(R_5 + R_8\right) n_{Xe^*(1s_3)}\right] n_e m_{Xe} V_c \Delta t, \tag{5}$$

$$\Delta m_{Xe^+} = \left[R_6 n_{Xe} + R_7 n_{Xe^*(1s_5)} + R_8 n_{Xe^*(1s_3)}\right] n_e m_{Xe} V_c \Delta t, \tag{6}$$

where m_{Xe} is the atomic mass of Xe. If the mass increment is positive, new macroparticles are created in the cell. In this case, $\Delta m > 0$, a population control algorithm is applied to decide the weight of new macro-particles, while a uniform distribution sampling in the cell is applied for the position and a Maxwellian

distribution sampling (defined with the properties of the heavy species before collisions) is applied for the velocity.[34] If macroparticles of a species need to be eliminated, $\Delta m < 0$, a weight reduction proportional to their initial weight is applied to all macroparticles of that species in the cell. All heavy species hitting a wall are reflected back with an energy fully accommodated to the wall, and an angle given by the Schamberg's model.[35] Upon wall collision, the chemical state may also change: Xe remains as Xe; $Xe^*(1s_5)$ and $Xe^*(1s_3)$ are de-excited to Xe; and Xe^+ is recombined to Xe.

The fluid model[33,36] is quasineutral, magnetized and drift-diffusive and considers the particle mass, momentum, and energy conservation, and the heat flux equations. An unmagnetized, collisionless sheath model defines the boundary conditions in terms of electron currents and energy fluxes. The plasma chemistry introduces source/sink terms in the particle and energy conservation equations, S_e and P'''_{inel}, and resistive terms in the momentum and heat flux equations, $\boldsymbol{F}_{res}$ and $\boldsymbol{Y}_{res}$. These terms are defined as

$$S_e = n_e \sum_c \nu_{ec} \Delta Z_c, \tag{7}$$

$$P'''_{inel} = n_e \sum_c \nu_{ec} \varepsilon_{thc}, \tag{8}$$

$$\boldsymbol{F}_{res} = m_e n_e \sum_c \nu_{ec} \left(\boldsymbol{u}_{sc} - \boldsymbol{u}_e \right), \tag{9}$$

$$\boldsymbol{Y}_{res} = -\frac{m_e \nu_e}{e} \boldsymbol{q}_e, \tag{10}$$

where ΔZ_c is the number of electrons generated in the collision process c, whose frequency is $\nu_{ec} = R_c n_{sc}$, n_{sc} and $\boldsymbol{u}_{sc}$ are the density and velocity of the colliding heavy species s (again for the collision process c); and $\nu_e = \sum_c \nu_{ec}$ is the total electron collision frequency. The anomalous transport in momentum and heat flux for cross-field diffusion and parallel-field cooling are accounted for with a simple phenomenological model introducing additional collision terms to $\boldsymbol{F}_{res}$ and $\boldsymbol{Y}_{res}$.[33] These terms are based on two parameters α_{ano} for cross-field diffusion, and ν_q for parallel-field cooling.

In order to avoid numerical diffusion the equations are solved on a magnetic field aligned mesh.[36] For spatial discretization, a finite volume method is applied for the conservation equations, and a finite difference method is applied for momentum and heat flux equations. For time discretization, a semi-implicit scheme is applied.

C. Simulation set-up

Figure 2 shows the sketch of the virtual EPT to be simulated with HYPHEN, which is the same used in Refs. 25, 33 and similar to an existing prototype thruster.[6] The thruster chamber has a radius $R = 1.25$

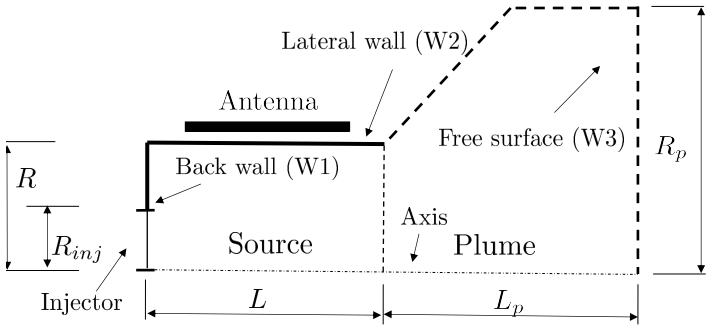

Figure 2. Sketch of the virtual EPT thruster.

cm and a length $L = 3$ cm. The magnetic circuit has two coils and generates a stationary magnetic field. It is quasi-axial inside the source and divergent outside in the plume with the maximum strength, about 1200 G, in the middle of the chamber (see Fig. 3(b) in Ref. 33). The antenna is assumed to operate in a mode so that the power deposition map P'''_a is Gaussian (see Fig. 3(c) in Ref. 33) with the maximum density at

the center of the chamber $(z, r) = (-3, 0)$ cm. Its integral over the domain gives the total power absorbed by the plasma as $P_a = \int_{\Omega_p} P_a''' d\Omega$. The injector, which is circular with radius $R_{inj} = 0.625$ cm and on the back surface of the chamber, injects a propellant mass flow rate of $\dot{m}$ with mean velocity $u_{inj} = 400$ m/s and temperature $T_{inj} = 0.03$ eV. Simulations are run with a nominal power of $P_a = 100$ W and different mass flow rates to search for the operational regimes where stepwise ionization can be important.

The simulation domain contains the thruster chamber (W1 is the back wall and W2 is the lateral wall) and the plume (W3 is the downstream free loss surface). The plume has a conical shape, with a length $L_p = 12$ cm and a maximum radius $R_p = 5$ cm. The numerical (meshes and time steps) and physical parameters for anomalous transport, $\alpha_{ano} = 0.02$ and $\nu_q = 5 \cdot 10^8$ s^{-1}, are the same as in Refs. 25,33. The total simulation time is 1.5 ms, and the results shown in the following section correspond always to such a simulation time, which assures the steady state.

III. Analysis of plasma generation and stepwise ionization

The ratio between power and mass flow controls the electron temperature and determines the relative importance between direct and stepwise ionization. Figure 3 (a) shows the mean value of T_e over the plasma source volume, $\overline{T}_e$, for $P_a = 100$ W and versus $\dot{m}$, in the range 0.1-10 mg/s. The curve $\overline{T}_e(\dot{m})$, as expected, decays with $\dot{m}$: it starts being 21.8 eV at $\dot{m} = 0.1$ mg/s, and decays to < 3.5 eV at $\dot{m} > 1$ mg/s. At low T_e, about 1-2 eV, the rate of excitation to the metastable states becomes significant against that of direct ionization according to Fig. 1.

Figure 3 (b)-(e) show the amount of ions generated and the contribution of stepwise ionization. Panel (b) shows the total amount of ion mass generated per unit time via the ionization processes, which is given by

$$\dot{m}_i = \int_{\Omega_p} \left(R_{dion} n_{Xe} + R_{sion1} n_{Xe^*(1s_5)} + R_{sion2} n_{Xe^*(1s_3)} \right) n_e m_{Xe} d\Omega. \tag{11}$$

The curve $\dot{m}_i(\dot{m})$ grows to reach a maximum value of about $\dot{m}_i = 2.88$ mg/s at $\dot{m} = 1$ mg/s and then saturates since no more power is available to ionize the increasingly injected propellant. The ions generated are from direct ionization $\dot{m}_{dion} = \int_{\Omega_p} \left(R_{dion} n_{Xe} \right) n_e m_{Xe} d\Omega$, and stepwise ionization $\dot{m}_{sion} = \int_{\Omega_p} \left(R_{sion1} n_{Xe^*(1s_5)} + R_{sion2} n_{Xe^*(1s_3)} \right) n_e m_{Xe} d\Omega$. Panel (c) shows the percentage of ion generation via the stepwise ionization. It starts from very low values for low $\dot{m}$, 1% for $\dot{m} = 0.1$ mg/s, and then grows monotonically until becoming comparable to direct ionization for high $\dot{m}$; 5.7% for $\dot{m} = 0.5$ mg/s, 14.7% for $\dot{m} = 1$ mg/s, 23.1% for $\dot{m} = 2.5$ mg/s and 33.4% for $\dot{m} = 10$ mg/s. For high $\dot{m}$, without stepwise ionization, the plasma discharge would fade rapidly. The contribution from $Xe^*(1s_5)$ is almost double as large as that from $Xe^*(1s_3)$.

Panel (d) then shows the total metastable neutral mass rate generated in the volume,

$$\dot{m}_{nm} = \int_{\Omega_p} \left(R_{excm1} + R_{excm2} \right) n_{Xe} n_e m_{Xe} d\Omega. \tag{12}$$

The curve $\dot{m}_{nm}(\dot{m})$ also grows monotonically, being $\dot{m}_{nm} = 0.008$ mg/s for $\dot{m} = 0.1$ mg/s, $\dot{m}_{nm} = 0.15$ mg/s for $\dot{m} = 0.5$ mg/s and $\dot{m}_{nm} = 0.94$ mg/s for $\dot{m} = 10$ mg/s. From mass conservation, i.e. equating the source and sink terms of metastable neutrals, we have that $\dot{m}_{nm} = \dot{m}_{sion} + \dot{m}_{deexc,coll} + \dot{m}_{deexc,wall}$, where $\dot{m}_{deexc,coll}$ is the mass rate of metastable neutrals de-excited via collisions, and $\dot{m}_{nm,wall}$ is that of metastable neutrals de-excited at the walls. Panel (e) shows the fraction of metastable neutrals that are lost by either stepwise ionization ($\dot{m}_{sion}$) and de-excitation ($\dot{m}_{deexc,wall}$) at the walls. The stepwise ionization is larger than 88% in the whole range of $\dot{m}$. The remaining fraction is from de-excitation, and is mainly due to wall de-excitation, being collisional de-excitation negligible.

IV. Analysis of the impact on the plasma discharge

First, the effects of the stepwise ionization on the thruster performance are discussed. Several useful efficiencies are defined based on the ion mass flow and power balances, which in the steady state are[33]

$$\dot{m}_i = \dot{m}_{i,wall} + \dot{m}_{i,beam}, \tag{13}$$

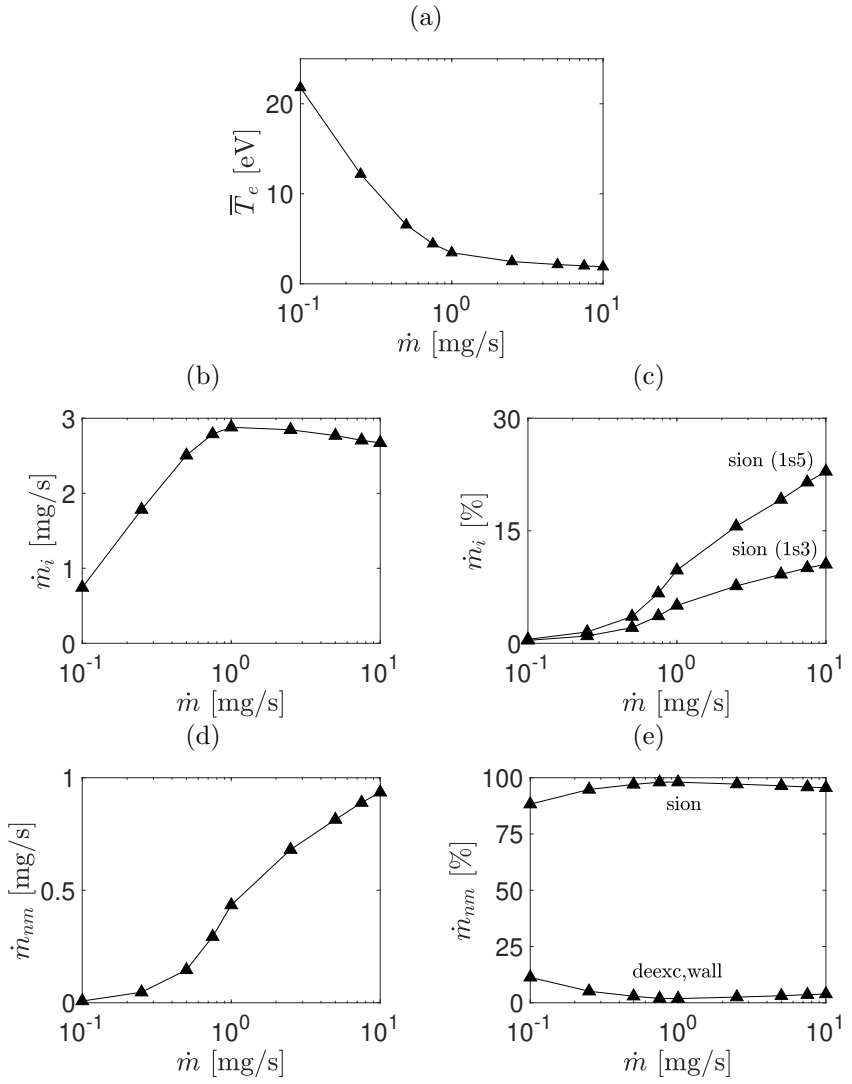

Figure 3. (a) Mean source electron temperature. (b) Total ion mass flow generated (c) and percentage of stepwise ionization for the two metastable states. (d) Total metastable neutral mass flow generated and (e) and percentage of stepwise ionization and wall deexcitation. Curves are shown vs $\dot{m}$ for $P_a = 100$ W.

and

$$P_a = P_{inel} + P_{wall} + P_{beam}. \tag{14}$$

In these expressions, $\dot{m}_{i,wall}$ and P_{wall} are the ion mass flow and plasma energy flow to the thruster walls (W1+W2), respectively; $\dot{m}_{i,beam}$ and P_{beam} are those across the downstream free loss surface (W3); and P_{inel} is the power sink due to inelastic collisions. The propellant mass utilization and the ion production efficiency are defined, respectively, as

$$\eta_u = \dot{m}_{i,beam}/\dot{m}, \qquad \eta_{prod} = \dot{m}_{i,beam}/\dot{m}_i. \tag{15}$$

The thrust efficiency is defined and factorized as

$$\eta_F = \frac{F^2}{2\dot{m}P_a} \equiv \eta_{ene}\eta_{div}\eta_{disp}, \tag{16}$$

with

$$\eta_{ene} = \frac{P_{beam}}{P_a}, \qquad \eta_{disp} = \frac{F^2}{2\dot{m}P_{beam}^{(z)}}, \qquad \eta_{div} = \frac{P_{beam}^{(z)}}{P_{beam}}, \tag{17}$$

respectively, the energy, plume-dispersion and plume-divergence efficiencies. Here F and $P_{beam}^{(z)}$ are the thrust and the plasma axial energy flow downstream. (Notice that in the definition of η_F, P_a is the power absorbed by the plasma, and the actual power consumed is the one emitted by the antenna, which is higher due to the reflection and transmission losses).

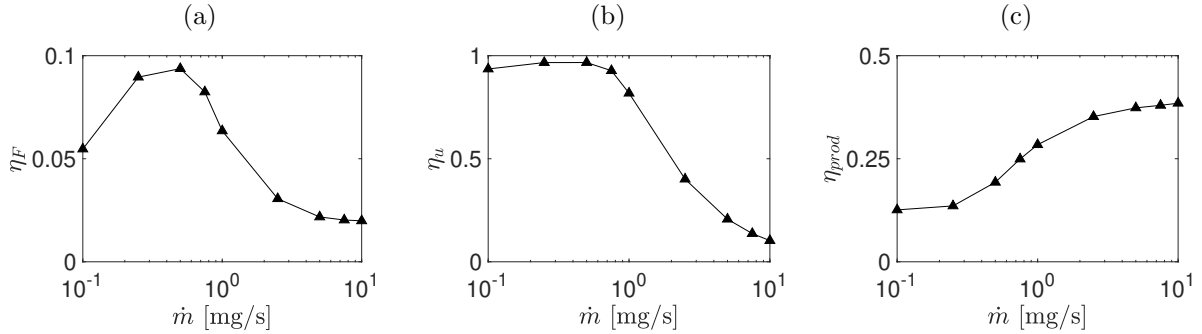

Figure 4. (a) Thrust efficiency, (b) propellant utilization efficiency and (c) production efficiency vs $\dot{m}$ for $P_a = 100$ W.

Figure 4 shows η_F, η_u and η_{prod} vs $\dot{m}$. The curve $\eta_F(\dot{m})$ [panel (a)] is maximum at $\dot{m} = 0.5$ mg/s being $\eta_F = 9.4\%$. For this operation point, there is nearly full ionization with $\eta_u = 97\%$ but there is significant plasma recombination at the walls with $\eta_{prod} = 19\%$. At high $\dot{m}$, the power is not enough to ionize all the injected propellant, and $\eta_u(\dot{m})$ [panel (b)] decays. At low $\dot{m}$, there is more wall recombination, and $\eta_{prod}(\dot{m})$ [panel (c)] reduces further. In the regime where stepwise ionization is significant, say $\dot{m} \geq 1$ mg/s (Fig. 3 (b)), $\eta_F < 6.4\%$ due to the low electron temperature and incomplete ionization. Many real prototypes in the literature currently are not optimized and could fall within this regime.

Table 3 shows, in detail, all the efficiencies for an operational point at $\dot{m} = 2.5$ mg/s. Two cases are shown, without and with stepwise ionization (for the former, the collisional processes 2, 3, 4, 5, 7 and 8 of Table 2 are not included in the simulation). In the case without stepwise ionization, the thrust efficiency is $\eta_F = 2.5\%$. The ionization is incomplete, $\eta_u = 34.1\%$, and the energy efficiency is low $\eta_{ene} = 9.6\%$; most of the power is lost in inelastic collisions $P_{inel}/P_a = 75.5\%$, mainly in excitation (about 2/3) due to the low electron temperature. Regarding the plume, the dispersion efficiency is also low, $\eta_{disp} = 0.34$, due to the presence of a large amount of slow neutrals. If stepwise ionization is accounted for, on the other hand, the thrust efficiency is higher, $\eta_F = 3.1\%$, the ion production is improved and η_u is 15% relatively higher. This affects mainly η_{ene}, which is 9% higher due to the lower power losses in inelastic collisions (the excitation energy to the metastable states is not completely lost); and η_{disp}, which is 8% higher.

Stepwise ionization	$\dot{m}$ [mg/s]	P_a [W]	$\dot{m}_i$ (meta) [%]	F [mN]	η_F	η_{ene}	η_{disp}	η_{div}	η_u	η_{prod}	P_{wall}/P_a	P_{inel}/P_a
No	2.5	100	-	3.53	0.025	0.096	0.34	0.77	0.341	0.350	0.149	0.755
Yes	2.5	100	23.1	3.91	0.031	0.106	0.37	0.77	0.401	0.352	0.163	0.731

Table 3. Performance figures for a fixed operational point, with and without stepwise ionization.

Figure 5 shows the 2D maps of plasma magnitudes for the operational point at $\dot{m} = 2.5$ mg/s. Electron temperature [panel (b)] peaks at about 2.6 eV, around the central section of the chamber, and then it decays by only around 0.5 eV in the chamber and 1 eV in the plume. The electric potential [panel (a)] is nearly constant in the radial direction and drops in the axial one by around $3T_e$, from source to plume. The neutrals at the ground state [panel (c)] are depleted; n_n is maximum near the injection surface, with $n_{Xe} \approx 3.5 \cdot 10^{20}$ m^{-3}, and it drops by one order of magnitude along the chamber length. The maximum plasma density [panel (d)], about $n_e \approx 3 \cdot 10^{19}$ m^{-3}, is found close to the center of the chamber. The mean free path for direct ionization inside the chamber is $\lambda_{dion} = u_n/(R_{dion} n_e) \sim$ 2-6cm, which explains the behavior of n_n and n_e (the chamber length is 6 cm). The generated ions are driven by the electric potential gradient, and a portion is lost at the walls and recombined there as seen in the growth of n_{Xe}. Because of this wall recombination,

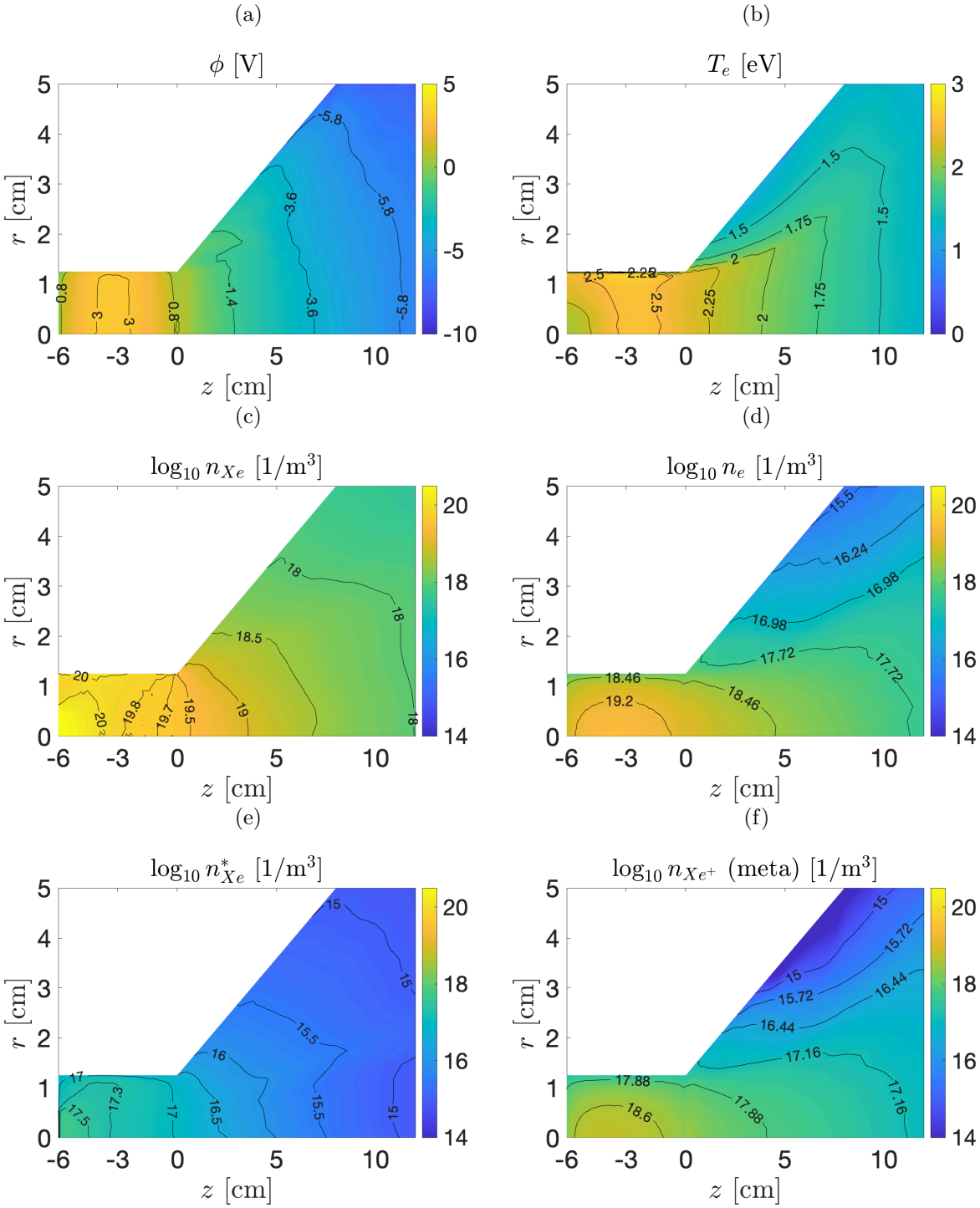

Figure 5. 2D maps of neutral and ion densities for the operation point $\dot{m} = 2.5$mg/s and $P_a = 100$W.

in the plume there is an incomplete ionization, with $n_{Xe} > n_e$. The production rate of metastable neutrals is mainly proportional to n_{Xe} given the quasi-uniform profile of T_e, and away from the walls their density profile [panel (e)] is very similar to that of n_{Xe}; near the walls, metastable neutrals are de-excited, and n^*_{Xe} is smaller than n_{Xe}. The magnitude of n^*_{Xe} is very low, about two orders of magnitude smaller than n_{Xe}. The mean free paths inside the chamber for excitation to metastable states and stepwise ionization are $\lambda_{excm}/\lambda_{dion}$ = 2-4 and $\lambda_{sion}/\lambda_{dion}$ = 1-5·10^{-3}, which suggests that excitation to metastable states is less probable than direction ionization, but once excited the ionization is nearly assured. The density of ions

from stepwise ionization features a profile [panel (f)] similar to that of n_e as expected due to the similarity between n_{Xe} and n^*_{Xe}, and it is about 40% of n_e.

Figure 6 shows the normalized axial velocity distribution functions on the axis for ions generated by direct ionization from neutrals at the ground state, and ions by stepwise ionization from neutrals at the metastable states. The Maxwellian distribution functions for ion-ground population based on its local magnitudes are also plotted. Two locations are studied, one at $z = -3$ cm (inside the chamber) and one at $z = 10$ cm (in the plume). The ion-ground population mean velocity at $z = -3$ cm is $u_{iz} = 0.3$ km/s, while at $z = 12$ cm it is $u_{iz} = 3.4$ km/s (equivalent to an energy of about 8 eV, and according to the potential decay). At $z = -3$ cm, the distribution is very close to a Maxwellian. At $z = 10$ cm, after being shaped by the potential decay, the velocity distribution deviates from a Maxwellian being more monoenergetic and with the peak displaced slightly above the mean velocity. The ion-metastable populations have nearly the same distributions as those produced from ionization of ground state neutrals, which is a consequence of the proportionality of their density profiles.

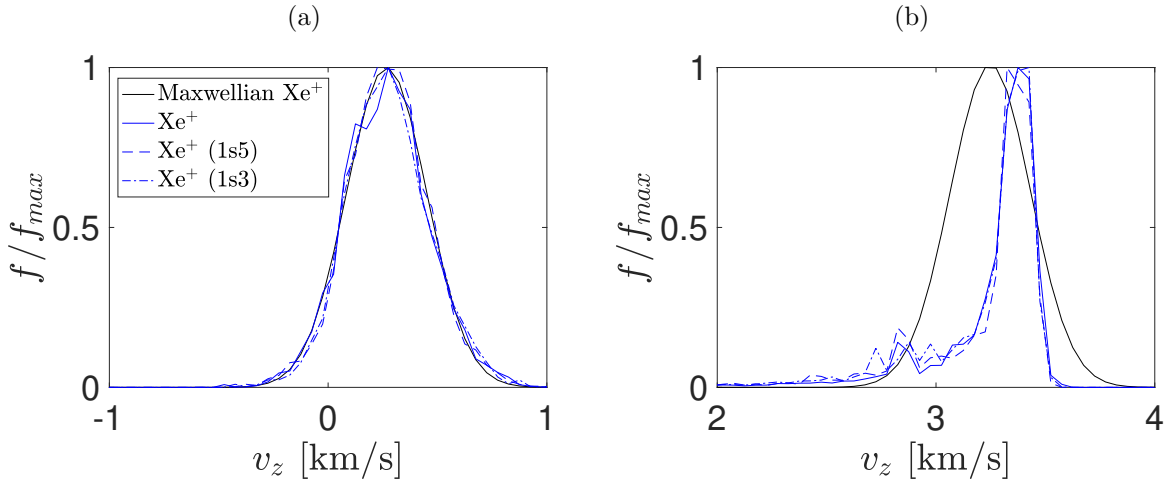

Figure 6. Axial velocity distribution functions (normalized) on the axis at (a) $z = -3$ cm and (b) $z = 10$ cm for ions generated from neutral ground state (——) and metastable states $1s_5$ (- - - -) and $1s_3$ (-.-.-.-.). Maxwellian distribution function for ions-ground population (——) is also plotted with the local temperature and mean velocity ($T_i = 0.046$ eV and $u_{iz} = 0.3$ km/s at $z = -3$ cm, $T_i = 0.043$ eV and $u_{iz} = 3.4$ km/s at $z = 10$ cm).

V. Conclusions

The impact of stepwise ionization in the operation of EPTs is assessed. The plasma chemistry of the metastable states for xenon, $1s_5$ and $1s_3$, is implemented in the hybrid 2D axisymmetric simulation code HYPHEN. Among the electronic excitation states, the radiative ones are assumed to de-excitate to the ground state instantaneously, and the corresponding energy loss is considered in the electron energy balance of the fluid model. The metastable states, on the other hand, are tracked with dedicated particle lists in the PIC model. The main collisions between electrons and heavy species for metastable neutrals are implemented: excitation from the ground state, de-excitation and ionization from the metastable states. These collisions are modeled with Monte Carlo collision methods, which generate or remove macroparticles. The interaction of the metastable neutrals with the walls is also modeled, and they naturally de-excite to the ground state, upon collision with the material.

The assessment of the stepwise ionization effects is carried out for a virtual EPT, operated with a nominal power of 100 W and varying the mass flow between 0.1 mg/s and 10 mg/s. The mass flow controls the electron temperature and in turn the amount of stepwise ionization, decreasing and increasing respectively with it. The electron temperature and amount of ions from stepwise ionization are below 3.5 eV and above 14.7% respectively for mass flows larger than 1 mg/s. The metastable neutrals, once produced, are mostly ionized (more than 88%), while the rest is de-excitated at the walls; de-excitation via collisions with electrons is found to be negligible.

Analyzing the performances, the maximum thrust efficiency is at 0.5 mg/s with a value of 9.4%. At lower

and higher mass flows, the plasma recombination at the walls and the incomplete ionization, respectively, reduces the thrust efficiency. At the operational point of maximum thrust efficiency, with a high electron temperature and full ionization, the stepwise ionization is negligible. Instead, for a mass flow of 2.5 mg/s, the amount of ions from stepwise ionization is 23.1%. By comparing simulations with and without stepwise ionization, it is found that the stepwise ionization contributes to a 15% increase of the propellant utilization, and reduces the power losses in inelastic collisions giving rise to a higher thrust efficiency. The 2D maps for the plasma magnitudes show that metastable neutral density is very low, about two order of magnitudes lower than that of ground neutrals. Typical densities and temperatures inside the thrust chamber suggest that the mean free path for stepwise ionization is much smaller than that for direct ionization, and the thruster chamber length. Given the quasi-uniform electron temperature profile, the density profile and velocity distribution function of ions from stepwise ionization are very similar to the ones of those from direct ionization.

As future work, it is planned to assess the impact of stepwise ionization for other EP technologies, in particular for Hall effect thrusters. Despite reaching higher maximum electron temperatures, there are locations with cool electrons near the anode, where stepwise ionization could be important. In addition, the temperature profile is more complex being highly non-uniform along the thruster chamber, which may lead to different velocity distribution functions of ions from stepwise ionization and direct ionization.

Acknowledgments

This research was supported by the Spanish Government, under the HEEP project, Grant No. PID2022-140035OB-I00. J. Zhou was also supported by the program *Recualificación del Sistema Universitario Español, Margarita Salas*, of the Ministerio de Universidades (Spanish Government).

References

[1]I. Levchenko, S. Xu, S. Mazouffre, D. Lev, D. Pedrini, D. Goebel, L. Garrigues, F. Taccogna, and K. Bazaka. Perspectives, frontiers, and new horizons for plasma-based space electric propulsion. *Physics of Plasmas*, 27(2):020601, 2020.

[2]D.M. Goebel and I. Katz. *Fundamentals of Electric Propulsion: Ion and Hall Thrusters*. Jet Propulsion Laboratory, Pasadena, CA, 2008.

[3]Kazunori Takahashi, Christine Charles, Rod Boswell, and Akira Ando. Performance improvement of a permanent magnet helicon plasma thruster. *Journal of Physics D: Applied Physics*, 46(35):352001, 2013.

[4]Shunjiro Shinohara, Hiroyuki Nishida, Takao Tanikawa, Tohru Hada, Ikkoh Funaki, and Konstantin P Shamrai. Development of electrodeless plasma thrusters with high-density helicon plasma sources. *IEEE Transactions on Plasma Science*, 42(5):1245–1254, 2014.

[5]F. Trezzolani, M. Manente, E. Toson, A. Selmo, D. Moretto, M. Magarotto, F. Bos, P. De Carlo, D. Melazzi, and D. Pavarin. Development and testing of a miniature helicon plasma thruster. In *35th International Electric Propulsion Conference, Atlanta, GA, IEPC-2017-519*, 2017.

[6]J Navarro-Cavallé, M Wijnen, P Fajardo, and E Ahedo. Experimental characterization of a 1 kw helicon plasma thruster. *Vacuum*, 149:69–73, 2018. https://doi.org/10.1016/j.vacuum.2017.11.036 doi:10.1016/j.vacuum.2017.11.036.

[7]J.C. Sercel. *An experimental and theoretical study of the ECR plasma engine*. PhD thesis, California Institute of Technology, 1993.

[8]Á. Sánchez-Villar, F. Boni, V. Désangles, J. Jarrige, D. Packan, E. Ahedo, and M. Merino. Comparison of a hybrid model and experimental measurements for a dielectric-coated coaxial ECR thruster. *Plasma Sources Science and Technology*, 32(1):014002, 2023. https://doi.org/10.1088/1361-6595/acb00c doi:10.1088/1361-6595/acb00c.

[9]M. Umair Siddiqui, C. Cretel, J. Synowiec, Andrea G. Hsu, Jason A. Young, and R. Spektor. First performance measurements of the phase four rf thruster. Paper IEPC-2017-431. 2017.

[10]K. Takahashi and A. Ando. Enhancement of axial momentum lost to the radial wall by the upstream magnetic field in a helicon source. *Plasma Physics and Controlled Fusion*, 59:054007, 2017.

[11]G. Parissenti, N. Koch, D. Pavarin, E. Ahedo, K. Katsonis, F. Scortecci, and M. Pessana. Non conventional propellants for electric propulsion applications. In *Space Propulsion 2010*, SP2010-1841086, San Sebastián, Spain, 2010.

[12]N. Bellomo, M. Magarotto, M. Manente, F. Trezzolani, R. Mantellato, L. Cappellini, D. Paulon, A. Selmo, D. Scalzi, M. Minute, M. Duzzi, A. Barbato, A. Schiavon, S. Di Fede, N. Souhair, P. De Carlo, F. Barato, F. Milza, E. Toson, and D. Pavarin. Design and in-orbit demonstration of regulus, an iodine electric propulsion system. *CEAS Space Journal*, 14:79–90, 2022. https://doi.org/10.1007/s12567-021-00374-4 doi:10.1007/s12567-021-00374-4.

[13]Y. Nakagawa, H. Koizumi, H. Kawahara, and K. Komurasaki. Performance characterization of a miniature microwave discharge ion thruster operated with water. *Acta Astronautica*, 157:294 – 299, 2019.

[14]F. Romano, Y.-A. Chan, G. Herdrich, C. Traub, and et al. Rf helicon-based inductive plasma thruster (ipt) design for an atmosphere-breathing electric propulsion system (abep). *Acta Astronautica*, 176:476–483, 2020. https://doi.org/10.1016/j.actaastro.2020.07.008 doi:10.1016/j.actaastro.2020.07.008.

[15]G.J.M. Hagelaar, J. Bareilles, L. Garrigues, and J.P. Boeuf. Two-dimensional model of a stationary plasma thruster. *Journal of Applied Physics*, 91(9):5592–5598, 2002.

[16]F. I. Parra, E. Ahedo, J. M. Fife, and M. Martínez-Sánchez. A two-dimensional hybrid model of the Hall thruster discharge. *Journal of Applied Physics*, 100(2):023304, 2006.

[17]Francesco Taccogna and Pierpaolo Minelli. Three-dimensional particle-in-cell model of Hall thruster: The discharge channel. *Physics of Plasmas*, 25(6):061208, 2018.

[18]M. Magarotto, D. Melazzi, and D. Pavarin. 3d-virtus: Equilibrium condition solver of radio-frequency magnetized plasma discharges for space applications. *Computer Physics Communications*, 247:106953, 2020.

[19]M.A. Lieberman and A.J. Lichtenberg. *Principles of plasma discharges and materials processing*. John Wiley and Sons, Hoboken, NJ, 2005.

[20]K. Hara. An overview of discharge plasma modeling for Hall effect thrusters. *Plasma Sources Science and Technology*, 28(4):044001, 2019.

[21]Y. Yamashita, R. Tsukizaki, and K. Nishiyama. Importance of stepwise ionization from the metastable state in electron cyclotron resonance ion thrusters. *Journal of Electric Propulsion*, 1:2, 2022.

[22]A. Sánchez-Villar, J. Zhou, M. Merino, and E. Ahedo. Coupled plasma transport and electromagnetic wave simulation of an ECR thruster. *Plasma Sources Science and Technology*, 30(4):045005, 2021. https://doi.org/10.1088/1361-6595/abde20 doi:10.1088/1361-6595/abde20.

[23]Pedro Jiménez, Jiewei Zhou, Jaume Navarro-Cavallé, Pablo Fajardo, Mario Merino, and Eduardo Ahedo. Analysis of a cusped helicon plasma thruster discharge. *Plasma Sources Science and Technology*, 32(10):105013, 2023. https://doi.org/10.1088/1361-6595/ad01da doi:10.1088/1361-6595/ad01da.

[24]Jesús Perales-Díaz, Adrián Domínguez-Vázquez, Pablo Fajardo, Eduardo Ahedo, Farbod Faraji, Maryam Reza, and Tommaso Andreussi. Hybrid plasma simulations of a magnetically shielded Hall thruster. *Journal of Applied Physics*, 131(10):103302, 2022. https://doi.org/10.1063/5.0065220 doi:10.1063/5.0065220.

[25]J. Zhou, F. Taccogna, P. Fajardo, and E. Ahedo. A study of an air-breathing electrodeless plasma thruster discharge. *Propulsion and Power Research*, submitted for publication.

[26]M. Hayashi. Bibliography of electron and photon cross sections with atoms and molecules published in the 20th century. Xenon. Technical report, National Institute for Fusion Science, 2003.

[27]Nist database. https://www.nist.gov/pml/atomic-spectra-database. Accessed: 2023-04-19.

[28]Biagi database. https://nl.lxcat.net. Accessed: 2019-10-23.

[29]H. A. Hyman. Electron-impact ionization cross sections for excited states of the rare gases (ne, ar, kr, xe), cadmium, and mercury. *Physical Review A*, 20:855–859, 1979.

[30]Hayashi database. https://nl.lxcat.net. Accessed: 2019-10-23.

[31]J.A. Bittencourt. *Fundamentals of plasma physics*. Springer, Berlin, Germany, 2004.

[32]K. Takahashi. Helicon–type radiofrequency plasma thrusters and magnetic plasma nozzles. *Reviews of Modern Plasma Physics*, 3:3, 2019. https://doi.org/10.1007/s41614-019-0024-2 doi:10.1007/s41614-019-0024-2.

[33]J. Zhou, A. Domínguez-Vázquez, P. Fajardo, and E. Ahedo. Magnetized fluid electron model within a two-dimensional hybrid simulation code for electrodeless plasma thrusters. *Plasma Sources Science and Technology*, 31(4):045021, 2022.

[34]A. Domínguez-Vázquez, F. Cichocki, M. Merino, P. Fajardo, and E. Ahedo. Axisymmetric plasma plume characterization with 2D and 3D particle codes. *Plasma Sources Science and Technology*, 27(10):104009, 2018. https://doi.org/10.1088/1361-6595/aae702 doi:10.1088/1361-6595/aae702.

[35]A. Domínguez-Vázquez, F. Cichocki, M. Merino, P. Fajardo, and E. Ahedo. On heavy particle-wall interaction in axisymmetric plasma discharges. *Plasma Sources Science and Technology*, 30(8):085004, aug 2021. https://doi.org/10.1088/1361-6595/ac1715 doi:10.1088/1361-6595/ac1715.

[36]Jiewei Zhou, Daniel Pérez-Grande, Pablo Fajardo, and Eduardo Ahedo. Numerical treatment of a magnetized electron fluid within an electromagnetic plasma thruster code. *Plasma Sources Science and Technology*, 28(11):115004, 2019.